

Chaotic Organic Crystal Phosphorescent Patterns for Physical Unclonable Functions

Healin Im, Jinsik Yoon, Jinho Choi, Jinsang Kim, Seungho Baek, Dong Hyuk Park,*
Wook Park,* and Sunkook Kim*

Since the 4th Industrial Revolution, Internet of Things based environments have been widely used in various fields ranging from mobile to medical devices. Simultaneously, information leakage and hacking risks have also increased significantly, and secure authentication and security systems are constantly required. Physical unclonable functions (PUF) are in the spotlight as an alternative. Chaotic phosphorescent patterns are developed based on an organic crystal and atomic seed heterostructure for security labels with PUFs. Phosphorescent organic crystal patterns are formed on MoS₂. They seem similar on a macroscopic scale, whereas each organic crystal exhibits highly disorder features on the microscopic scale. In image analysis, an encoding capacity as a single PUF domain achieves more than 10¹⁷ on a MoS₂ small fragment with lengths of 25 μm. Therefore, security labels with phosphorescent PUFs can offer superior randomness and no-cloning codes, possibly becoming a promising security strategy for authentication processes.

encryption key attract tremendous demands to offer to tighten the protection of personal information and privacy.^[1–3] To date, most secret keys and algorithms rely on software-based encryption key management, which has high risk of information extrusion. To overcome these weaknesses, hardware-based encryption key management such as a physical unclonable function (PUF) has been spotlighted as a promising alternative strategy. PUF provides impregnable security keys through the disordered physical features derived from deviations in the fabrication processes.^[4–10] The consequent physical randomness could offer individual keys such as a unique fingerprint, without external sources. Besides, it facilitates implementation with not only cost-effective and concise

1. Introduction

With the advances in smart technologies, the artificial-intelligence-based smart Internet of Things environment is invigorated in various fields from mobile to medical devices. Accordingly, security systems with an anti-counterfeiting

methods but also a high level of security.

There have been numerous PUF methods proposed.^[11] For example, static random access memory PUF (SRAM PUFs)^[12,13] utilizes insecure programmed states caused by the program disturb errors as PUF signals. Optical PUF^[4] exploits random speckle patterns attributed to the complicated interference by an inhomogeneous plastic shade. Edible PUF^[14] performs counterfeit medicines with different fluorescent proteins. Besides, quantum dot PUF^[15] demonstrates disordered flower-like patterns derived from an inkjet-print process. However, these approaches of PUF emerge limitations in the aspect of information capacity and integration with the existing security system.


Regarding the design of PUFs, a strategy should guarantee high randomness, miniaturization, simple fabrication, and superior data collection speed. In this regard, scalable organic crystal patterns are a powerful potential candidate as a random number generator. Organic crystal patterns are facile to manufacture by simple solution-based processes, including inkjet printing,^[16,17] solution spin casting,^[18] and solution drop-casting.^[19] Under in situ crystallization process, organic molecules are site-specifically nucleated and crystallized by surface treatments on the substrates^[20,21] to form the desired pattern on large scales. In contrast, individual organic crystals exhibit unexpected physical features such as size, morphology, and luminescence in micro scales, applicable for anti-counterfeiting encryption keys. Besides, each organic crystal pattern depends on the size of pre-defined area, possibly downsizing encryption keys and boosting the information capacity per unit area. Furthermore, simple spectrometers could observe organic crystal's

H. Im, S. Baek, S. Kim
School of Advanced Materials Science and Engineering
Sungkyunkwan University
Suwon-Si, Gyeonggi-do 16419, Republic of Korea
E-mail: seonkuk@skku.edu

J. Yoon, W. Park
Institute for Wearable Convergence Electronics
Department of Electronics and Information Convergence Engineering
Kyung Hee University
Deogyong-daero, Giheung-gu, Yongin-si
Gyeonggi-do 17104, Republic of Korea
E-mail: parkwook@khu.ac.kr

J. Choi, D. H. Park
Department of Chemical Engineering
Program in Biomedical Science & Engineering
Inha University
100 Inha-ro, Michuhol-gu, Incheon 22212, South Korea
E-mail: donghyuk@inha.ac.kr

J. Kim
Department of Materials Science and Engineering
University of Michigan
Ann Arbor, MI 48109, USA

 The ORCID identification number(s) for the author(s) of this article can be found under <https://doi.org/10.1002/adma.202102542>.

DOI: 10.1002/adma.202102542

luminescence characteristics with intuitive image analysis, enabling useful and high-speed data collection.

Herein, chaotic phosphorescent patterns are implemented by in situ crystallization of organic molecules and demonstrated for anti-counterfeiting codes of PUFs. Scalable MoS₂ films are synthesized by a two-step process^[22] and pre-patterned as a square shape with each length of 25 μm. Two types of organic crystal patterns are formed by the solution drop-casting on the pre-patterned MoS₂ films. Organic molecules are preferentially nucleated and crystallized on MoS₂ owing to the surface energy differences between MoS₂ and substrate. In addition, MoS₂ can optimize photophysical features of organic crystals at room temperature. Both organic crystals on MoS₂ exhibit phosphorescent emission at room temperature under ultraviolet (UV) light irradiations. Moreover, we have analyzed organic crystal micropatterns in digitization and cross-correlation to examine their randomness and encoding capacity as PUFs. For a precise analysis, the square-shaped MoS₂ pattern is defined as a unit area of a PUF. Furthermore, we have suggested the authentication processes of the proposed phosphorescent organic crystal patterns. As a result, it shows the potential to be the next generation PUFs as a core technology of encryption systems for the future.

2. Results and Discussions

Chaotic phosphorescent PUFs are demonstrated based on the inherent random features of organic crystals by in situ crystallization. **Figure 1a** illustrates an outline of the proposed PUF strategy. 2D security labels such as a quick response (QR) code or a bar code are designed in macroscopic scales for general authentication processes. The desirable 2D labels are composed of microscopic-scale organic crystals site-specifically grown on atomic seeds. In image analysis, the luminescence characteristics of disordered organic crystals are examined under UV light irradiations and translated as anti-counterfeiting keys. It could offer double-encryption for the general security labels, readily boosting security safety. Besides, each signal is collected in the form of luminescence, assuring no interference from residual dust.

Figure 1b illustrates in situ crystallization-based fabrication processes of emissive organic crystal patterns. Large area MoS₂ films are formed by a two-step method^[22] and patterned with a desirable design. Precursor solution with phosphorescent organic materials is drop-cast on as-prepared MoS₂ micropatterns and slowly evaporated under ambient conditions. In this

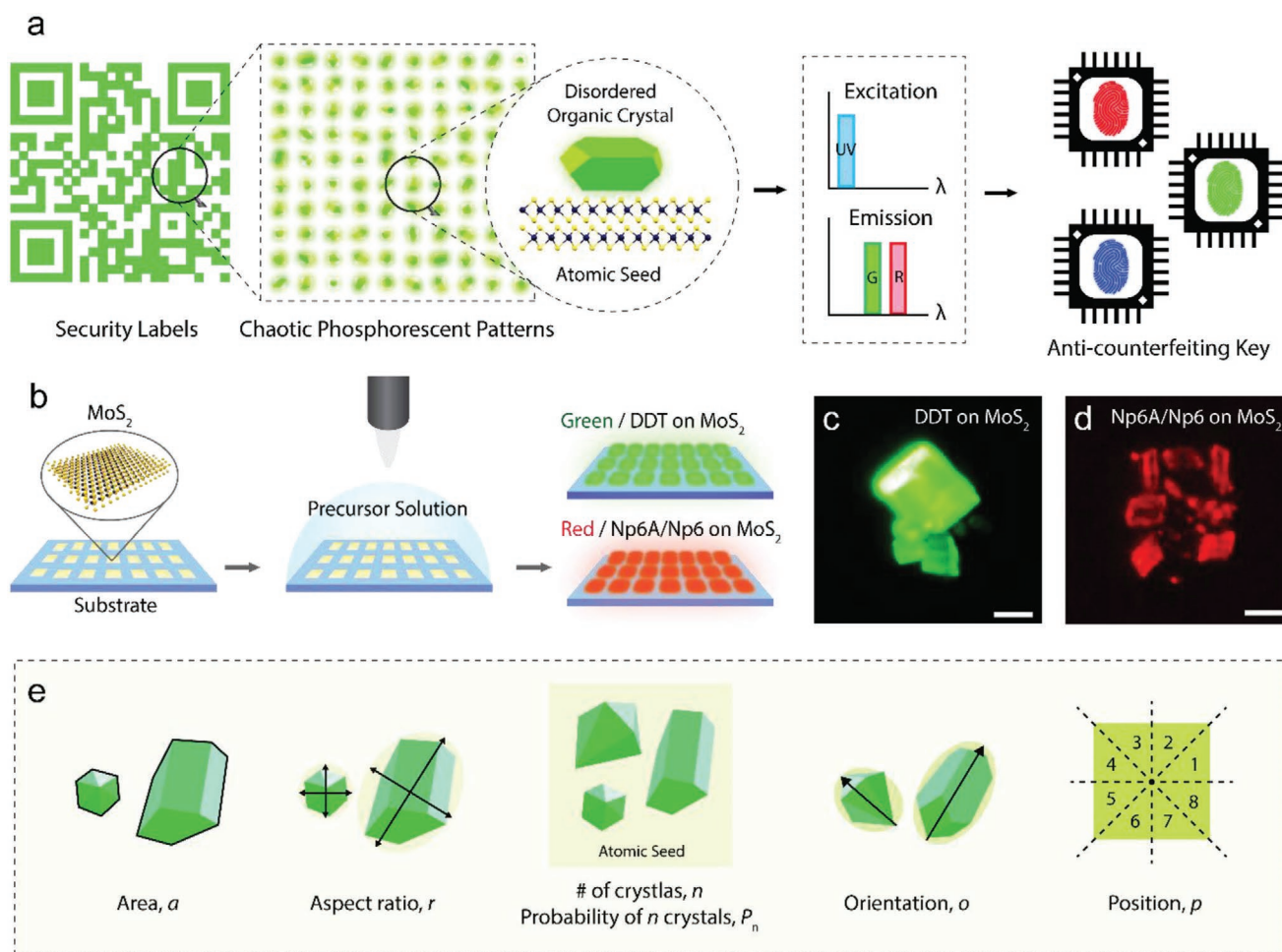


Figure 1. Outline of chaotic phosphorescent patterns for PUF. a) The proposed PUF strategy with the disordered phosphorescent organic crystal patterns. b) Overall fabrication process. c,d) CCD images of pure organic crystals of DDT (c) and Np6A/Np6 (d) on MoS₂ (scale bar: 10 μm). e) Parameter classification in organic crystals for digitization analysis.

work, 2,5-dihydroxyterephthalate (DDT) for green phosphorescence and 5-bromo-2,6-dihydroxy-1-naphthaldehyde (Np6A) and 1,5-dibromo-2,6-dihydroxynaphthalene (Np6) for red phosphorescence are utilized (see Figure S1, Supporting Information).^[23,24] Note that MoS₂ micropatterns as atomic seeds could modulate organic crystal formation.

Figure 1c,d shows charge-coupled device (CCD) images of DDT and Np6A/Np6 crystals on a single MoS₂ seed. Multiple organic crystals per MoS₂ seed are formed with random physical features such as size, shape, and location. We extract the features from the emission images and categorize them into 5 parameters: size, aspect ratio, orientation, position, and the number of crystals per MoS₂ seed. Area (*a*) is pixel components collected from the region where organic crystals emit light in the images. Then, a possible oval is assumed and calculated for each crystal. Based on the arbitrary ovals, aspect ratio (*r*), a minor axis/major axis ratio, and orientation (*o*) along the major

axis are defined. The number of organic crystals per atomic seed (*n*) and the probability of *n* crystals (*P_n*) are also classified. Besides, a single MoS₂ seed is divided into 8 regions every 45 degrees, and the position (*p*) of organic crystals is categorized. These parameters are used to estimate the possible encoding capacity of organic crystals/MoS₂ patterns.

To form discrete organic crystal patterns, MoS₂ should be used as pre-defined atomic seeds for PUF domains. Figure 2a illustrates the two-step method of scalable MoS₂ films. A few nanometer-scale Mo film is deposited by an RF sputter and annealed with H₂S gas at 1000 °C for 1 h, transforming Mo into MoS₂ films. The two-step grown MoS₂ films are characterized by Raman and X-ray photoelectron spectroscopy (Figure 2b,c). Raman spectrum of MoS₂ film emerges at 406.05 and 381.30 cm⁻¹ with a peak difference of 22.8 cm⁻¹, corresponding to the A_{1g} and E_{12g} modes of few-layer MoS₂.^[25] According to the XPS analysis, Mo⁴⁺ 3d_{5/2} and S²⁻ 2p_{3/2} appear at 229.7 and

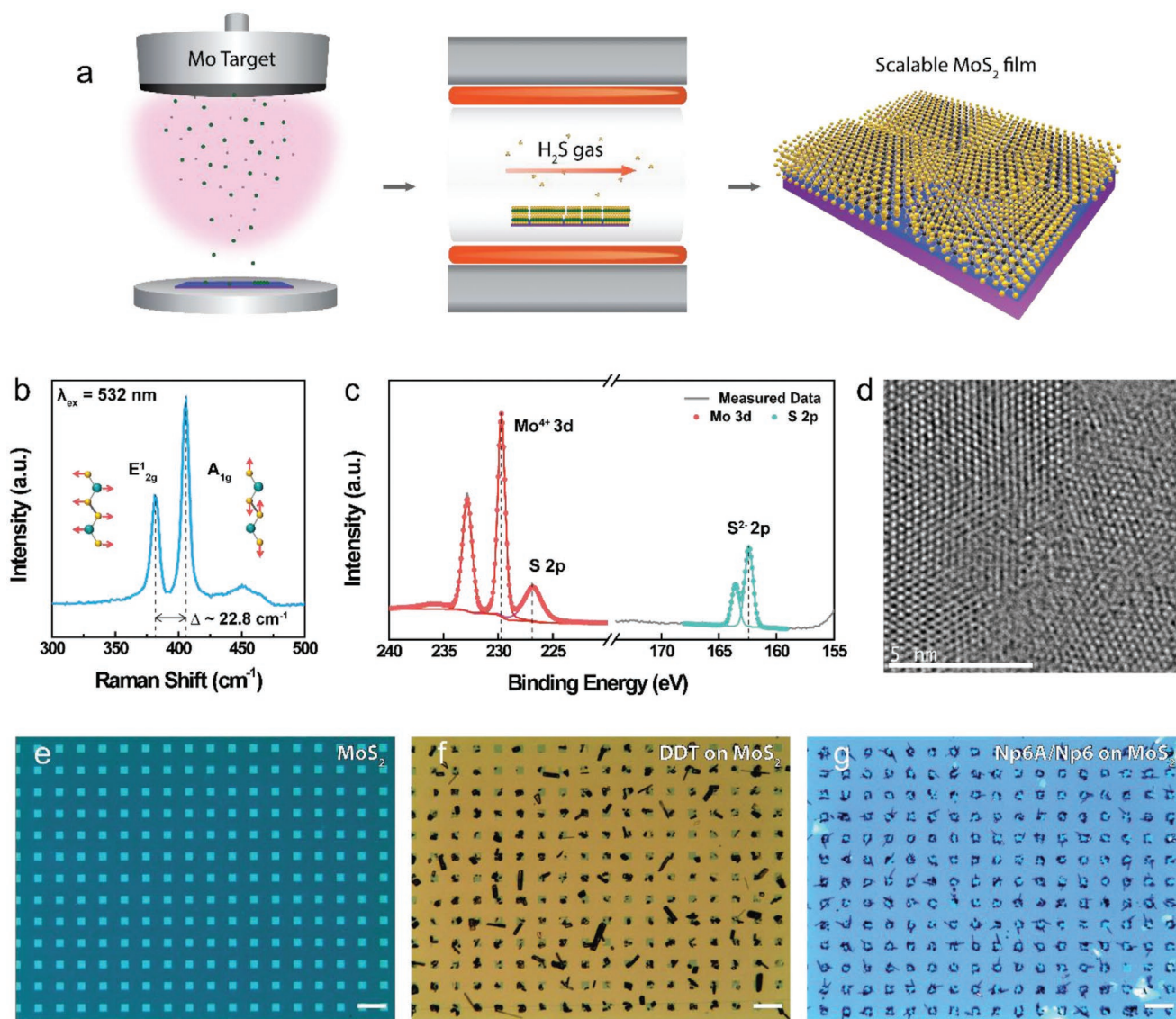


Figure 2. Scalable MoS₂ film. a) Two-step fabrication process. b) Raman analysis. c) XPS analysis. d) TEM image of MoS₂ film in plan view. e–g) Optical images of the patterned MoS₂ (e), DDT on MoS₂ (f), and Np6A/Np6 on MoS₂ (g) (scale bars: 100 μm).

162.4 eV, revealing the covalent bonds of Mo and S. In addition, the atomic structures of the MoS₂ films are examined by transmission electron microscopy (TEM). As shown in Figure 2d, the MoS₂ film is polycrystalline with multiple small grains of hexagonal lattice structures. In addition, partial Moiré patterns are attributed to the heterogeneity of the MoS₂ layer numbers.

Figure 2f–h shows the optical images of MoS₂, DDT/MoS₂, and Np6A/Np6/MoS₂ patterns. It demonstrates the well-formed discrete organic crystal patterns. To elucidate the preferential organic crystallization on MoS₂, contact angle analysis is performed for DDT and Np6A/Np6 solutions, as shown in Figure S2a,b, Supporting Information. Both solutions spread on the Si/SiO₂ substrate, resulting in undetectable contact angles. In contrast, DDT and Np6A/Np6 solutions show contact angles of $5.50 \pm 0.5^\circ$ and $6.56 \pm 0.1^\circ$, respectively, on large-area MoS₂ films, denoting that the surface energy differences between substrate and MoS₂. The site-specific growth of organic crystals may be attributed to the surface energy differences.^[20,26]

Moreover, it is observed that DDT crystals are site-specifically grown on different 2D materials such as MoSe₂, WS₂, and WSe₂ (Figure S3, Supporting Information). To establish the interaction between DDT molecular alignment and 2D materials, DDT molecules on the graphene surface are explored by scanning tunneling microscopy (STM). In Figure S4, Supporting Information, bright dots are occasionally attached to the well-arranged graphene honeycomb structure. These dots are benzene rings of DDT molecules, and the spacing between

dots is possibly alkyl chain distances. This indicates that DDT molecules may be aligned along the graphene lattices. Considering this phenomenon, we assume that this would occur on the hexagonal lattice structures of MoS₂. As aforementioned, two-step grown MoS₂ films comprise abundant small grains, achieving the disorder crystallization of DDT with multiple orientations and positions on the MoS₂ domains.

Next, the organic crystals are examined in the aspect of photophysical properties. Figure 3a shows photoluminescence (PL) spectra of DDT and Np6A/Np6 with and without MoS₂ seeds. Intrinsic DDT crystals emit blue fluorescence at a wavelength (λ_{em}) of 468 nm, whereas that on MoS₂ seeds show a clear redshift in PL peak with green phosphorescence at the λ_{em} of 511 nm. Meanwhile, a PL spectrum of Np6A/Np6 shows a weak fluorescent component at around λ_{em} of 449 nm and clear doublets at λ_{em} of 591 and 634 nm corresponding to the phosphorescent components. On the contrary, the fluorescent component of Np6A/Np6 crystal is considerably reduced on MoS₂ seeds. Each emission color is marked in the Commission International de L'Eclairage (CIE) coordinate diagram, as shown in Figure 3b. The inherent emissions at (0.1648, 0.2096) for DDT and (0.4401, 0.3048) for Np6A/Np6 are significantly shifted to (0.2714, 0.5250) and (0.5194, 0.3881) along with MoS₂ seeds, respectively. Furthermore, time-resolved PL spectra are measured at room temperature, and their lifetimes are extracted as shown in Figure 3c and Table 1. Both types of organic crystals on MoS₂ exhibit extensive lifetimes as compared to pristine status.

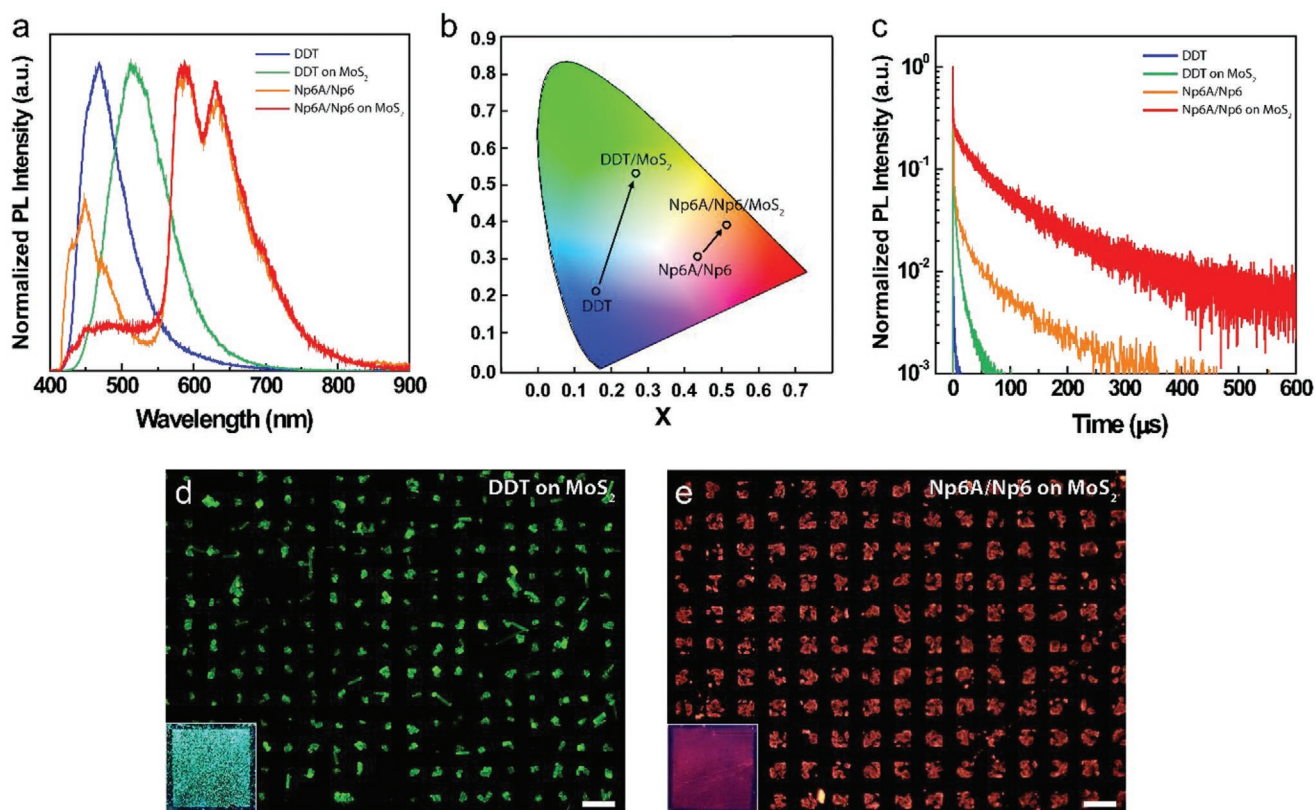


Figure 3. Photophysical properties of phosphorescent organic crystals. a) PL analysis, b) CIE chromaticity diagram, and c) time-resolved PL analysis of DDT, DDT on MoS₂, Np6A/Np6, and Np6A/Np6 on MoS₂. d,e) CCD images of DDT (d) and Np6A/Np6 (e) phosphorescent patterns (scale bar: 100 μ m). Insets of (d,e) are photographs of DDT and Np6A/Np6 patterns under a 365 nm lamp.

Table 1. Room-temperature lifetimes of organic crystals. The excitation wavelength (λ_{ex}) and emission wavelength (λ_{em}) are selected according to PL spectra.

Components	λ_{ex} [nm]	λ_{em} [nm]	Lifetime [μs]
DDT	355	470	< 1.27
DDT on MoS ₂	355	530	9.27
Np6A/Np6	375	600	86.17
Np6A/Np6 on MoS ₂	375	600	96.79

We implement further analysis to elaborate on the variations in photophysical features of organic crystals on MoS₂. Low-temperature PL analysis is performed for DDT and DDT/MoS₂ to confirm the origin of abrupt green luminescence of DDT/MoS₂. Under low-temperature conditions, most organic molecules lose their molecular vibration and deactivate the vibrational energy loss, resulting in the activation of phosphorescence.^[27,28] DDT is expected to suppress its molecular vibrations and promote the inherent phosphorescent features. Figure S5a,b, Supporting Information, presents temperature-dependent PL spectra of DDT and DDT/MoS₂. In DDT, broad doublets, possibly deconvolute into two discrete peaks at approximately 446 and 543 nm, emerge at 77 K. A newly formed PL peak at 543 nm may be attributed to the phosphorescence activation of DDT. In DDT/MoS₂, PL spectra are constant regardless of the surrounding temperature conditions, denoting that the phosphorescence of DDT is stabilized on MoS₂. Moreover, in Raman analysis (Figure S5c, Supporting Information), DDT/MoS₂ shows a significant peak shift at approximately 1328 cm⁻¹ (marked as *), indicating $n\pi^*$ triplet states of C=O.^[29–31] In Np6A/Np6 crystals, MoS₂ offers the ease condition for crystallization, stabilizing the red phosphorescences of Np6A/Np6 (Figure S6, Supporting Information).

Figure 3d,e shows CCD images of DDT/MoS₂ and Np6A/Np6/MoS₂ patterns. The luminescence images of organic crystal patterns achieve facile and intuitive image analysis. In these images, individual organic crystals are distinguishable from each other, readily sorting physical random features. In Figure 3d, most DDT crystals seem to be big and obtuse rhombohedron shapes. In Figure 3e, Np6A/Np6 crystals tend to show relatively small and random shapes. Moreover, Np6A/Np6 crystals own more individual fragments than the DDT crystals on a single MoS₂ seed. The macroscopic security labels seem almost identical from batch to batch, whereas the microscopic organic crystals are highly distinguishable and un-replicable. Such irregular micro-organic patterns are impossible to reproduce or copy.

Next, we have performed digitization analysis and 2D cross-correlation of chaotic phosphorescent patterns to evaluate the randomness and non-replicability. For high image analysis reliability, approximately 7000 DDT and 3000 Np6A/Np6 crystals (18 and 97k pixels, respectively) are collected and analyzed by a CCD camera. As shown in Figure 4 and Figure S7, Supporting Information, morphological features are mainly characterized into 5 parameters; area, aspect ratio, orientation, position, and the number of crystals per MoS₂ seed. These parameters are used as raw information to deduce the possible encoding capacity.

As shown in Figure 4, both DDT and Np6A/Np6 patterns show high randomness based on orientation and position with

a flat distribution of 5.6% and 12.5%. The remaining parameters (area, aspect ratio, and crystal number) exhibit clumped distributions. The orientation, position, crystal numbers, and probability are selected to extract the encoding capacity. The thresholds of orientations and position are 10° and 8 regions, respectively. In addition, we have extracted its possible random numbers in the ranges of more than 99% of real cases. Therefore, the encoding capacity (C_i) on a single MoS₂ seed with 25 μm lengths could be estimated by the following equation,

$$C_i = p \sum_n P_n \times o^n \quad (1)$$

where o , p , n , and P_n are the number of options derived from orientation, position, the number of crystals per MoS₂ seed, and the probability of forming n crystals. Thus, the producible C_i is 6.116×10^6 for DDT and 2.744×10^{17} for Np6A/Np6. Furthermore, if a security label is defined as an $A \times B$ array based on MoS₂ seeds, the group encoding capacity (C_g) could be exponentiated by the following equation.

$$C_g = (C_i)^{A \times B} \quad (2)$$

If a security label is designed in 1 mm² with abundant MoS₂ domains, C_g is around 10^{2700} and 10^{7000} for DDT and Np6A/Np6, respectively, showing the commercialization potential as promising PUF applications.

Furthermore, 2D cross-correlation analysis has evaluated the uniqueness of DDT and Np6A/Np6 patterns. Figure 5 presents the heatmaps and the histograms of cross-correlation values extracted from 480 4×4 DDT and 264 3×3 Np6A/Np6 PUF groups. In an identical crystal image (labeled as intra-distance distribution), the correlation is high, and the coefficient value is close to 1. In different crystal images (labeled as inter-distance distribution), the coefficient value is nearly 0. In addition, the cut-off threshold and false positive/negative rates are calculated by applying the mean (μ) and standard deviation (σ) to the Gaussian distribution function. Tables 2 to 7 present detailed values obtained from the cross-correlation of DDT and Np6A/Np6 patterns with different group sizes. 4×4 DDT group (Figure 5a,c) shows the false positive/negative rates of 5.248×10^{-58} and 2.732×10^{-55} , while 3×3 Np6A/Np6 group (Figure 5b,d) is 2.430×10^{-49} and 8.444×10^{-49} . Both groups are clearly divided with superior intercorrelation values, guaranteed as distinguishable patterns for PUF applications.

As aforementioned, conventional security labels such as QR codes or bar codes are designed with SW-based encryption algorithms. They are convenient and favorable for general authentication on macroscopic scales. However, SW-based labels are vulnerable to be counterfeited and stolen. On the contrary, security labels with un-replicable random microscale PUFs offer superior uniqueness and are nearly impossible to clone. We have proposed a highly secure and commercially available authentication process with phosphorescent PUF domains (Figure 6). At first, the desirable security labels with MoS₂ atom seeds are designed. Chaotic phosphorescent patterns based on organic crystals/MoS₂ are readily fabricated via solution drop-casting. As an image-based PUF manner, macropatterns such as QR codes or logos are screened by bare eyes, and then the chaotic phosphorescent patterns role in double encryption

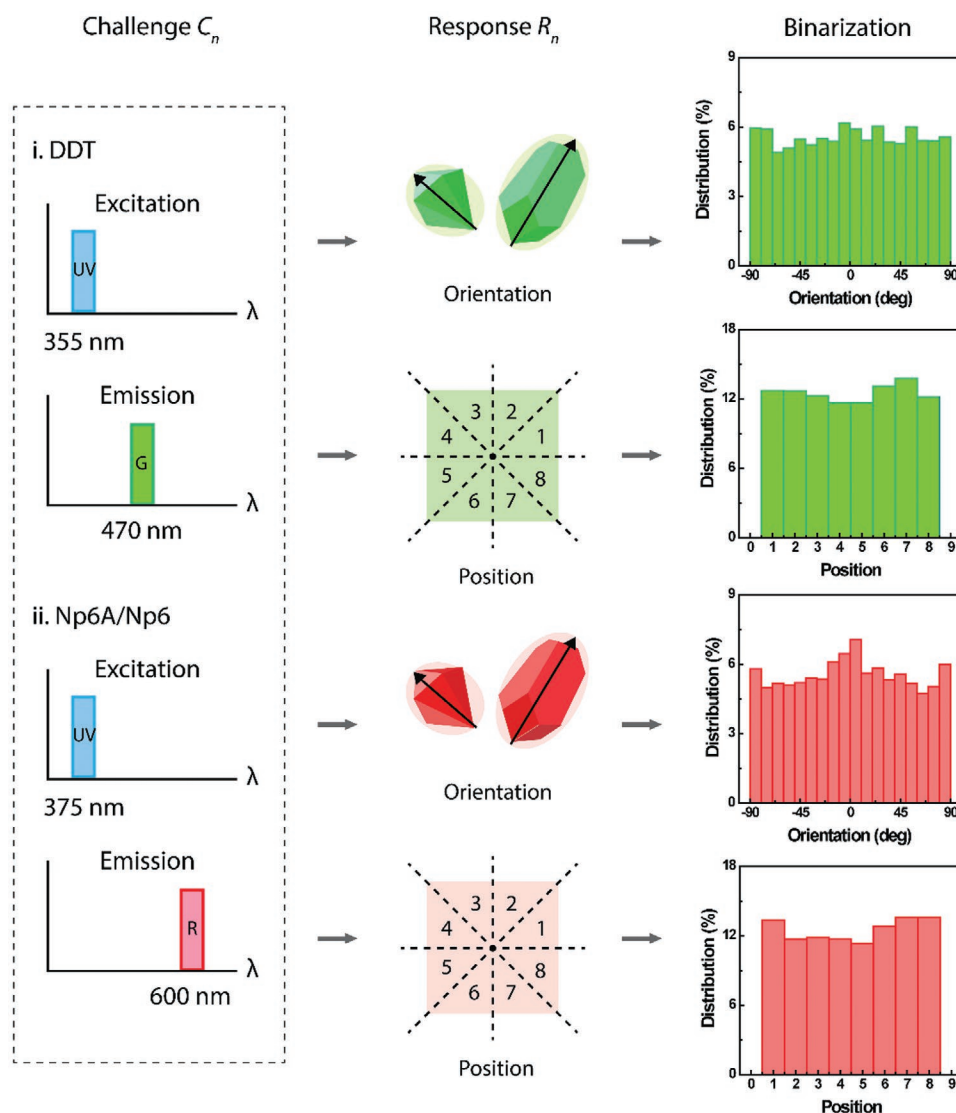


Figure 4. Flowchart of image analysis of chaotic phosphorescent patterns. At first, DDT and Np6A/Np6 crystals emit phosphorescence at wavelengths of 470 and 600 nm under UV light illumination. Based on the orientation and position of chaotic phosphorescent patterns, the randomness and the possible encoding capacity are statistically estimated.

keys. Pattern images are observed by affordable microscopic tools under UV light illumination. In evaluation, digitization and cross-correlation validate the randomness and estimate the encoding capacity of patterns. At this step, the images are obtained under different angles and distances to guarantee a decryption process. Each security label with PUFs is saved and processed in an AI database. Consequently, during the decoding processes, the security labels could perform the general authentication process to validate whether the label is real or fake.

3. Conclusions

Chaotic phosphorescent patterns are fabricated by in situ crystallization of pure organic crystals and demonstrated as anti-counterfeiting codes of PUFs. Organic molecules are site-specifically assembled and crystallized on MoS_2 seeds. Macroscopic phosphorescent patterns seem almost identical from

batch to batch, whereas the microscopic organic crystals are highly distinguishable and un-replicable. This offers double-security by forming the desirable security labels consisting of small PUF domains. Moreover, we have performed digitization analysis and 2D cross-correlation of chaotic phosphorescent patterns to estimate the encoding capacity. From a single PUF domain, the producible encoding capacity is 6.11×10^6 and 2.74×10^{17} for DDT and Np6A/Np6, respectively. This indicates that the security labels with phosphorescent PUFs could achieve superior randomness and the no-cloning codes, possibly commercializing. Therefore, chaotic phosphorescent patterns could be promising secure PUFs of the authentication process.

4. Experimental Section

Preparation of Phosphorescent Organic Crystal Patterns: For MoS_2 seed atoms, large area MoS_2 was synthesized by a two-step process.

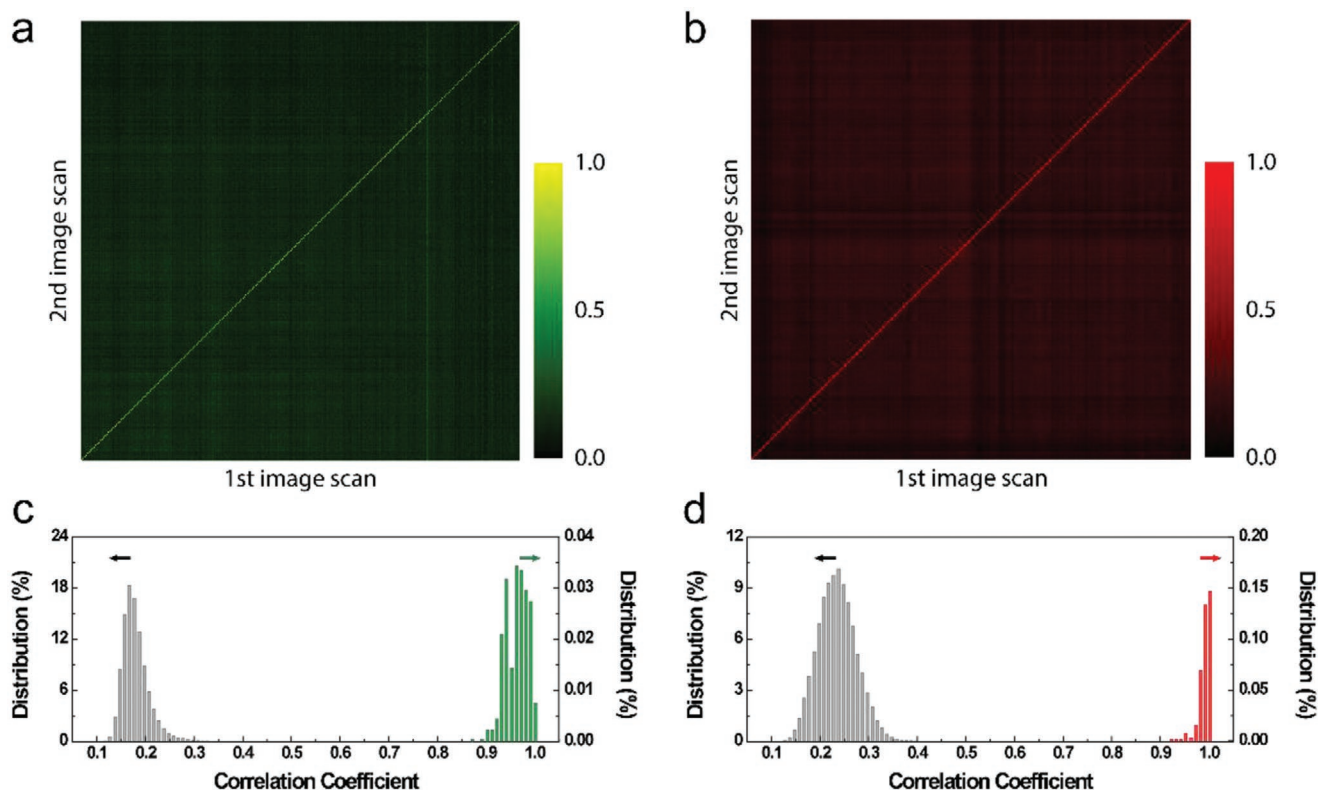


Figure 5. a–d) Heat maps and histograms of 2D cross-correlation values extracted from DDT (a,c) and Np6A/Np6 (b,d) patterns. Total data are obtained from 480 sets of 4×4 groups for DDT and 264 sets of 3×3 groups for Np6A/Np6.

At first, Mo film with a thickness of less than 2 nm was pre-deposited by RF sputter. The RF sputter and the deposition time were 150 W and 3 min, respectively. Then, Mo film was sulfurized by a gas-phase sulfur precursor H_2S at 1000 °C under the total gas flow condition of $\text{H}_2\text{S}:\text{H}_2:\text{Ar} = 1:50:5$, consequently forming uniform MoS_2 films. It was patterned as the desirable security label designs with small domains by photolithography.

For phosphorescent organic crystals, diethyl 2,5-dihydroxyterephthalate (97%, from Sigma Aldrich) was purchased and used without purification. 5-bromo-2,6-dihydroxy-1-naphthaldehyde and 1,5-dibromo-2,6-dihydroxynaphthalene were synthesized. The precursor solutions were prepared by adding them into dimethylformamide with a 1 mg mL^{-1} concentration and stirring at room temperature before the solution drop-casting. To produce security labels

with phosphorescent PUFs, the precursor solutions were dropped on the substrate with MoS_2 seeds under ambient.

Characterization: Scalable MoS_2 films were examined using a Raman spectrometer at λ_{ex} of 514 nm and an X-ray photoelectron spectrometer with a peak calibration at C 1s of 284.8 eV. A contact angle measurement observed the surface energy differences. A laser confocal microscope obtained the PL and the corresponding luminescent CCD images at λ_{ex} of 405 nm. Time-resolved photoluminescence (TRPL) measured organic crystals' lifetimes with impulse response function full-width half maximum of 240 ps at λ_{ex} of 375 nm.

Digitization Analysis: MATLAB SW has proceeded for image analysis. At first, the green (0, 1, 0) and the red (1, 0, 0) filters extracted the bright and the dark spots in luminescent images of DDT and Np6A/Np6 phosphorescent patterns. The threshold was defined by the “graythresh”

Table 2. Inter-distance distribution of DDT patterns.

Group size (samples)	1 × 1 (959)	2 × 2 (1098)	3 × 3 (880)	4 × 4 (480)	5 × 5 (300)
Mean (μ)	0.4866	0.3014	0.2160	0.1770	0.1513
Standard deviation (σ)	0.0716	0.0451	0.0313	0.0263	0.0244

Table 3. Intra-distance distribution of DDT patterns.

Group size (samples)	1 × 1 (959)	2 × 2 (1098)	3 × 3 (880)	4 × 4 (480)	5 × 5 (300)
Mean (μ)	0.9314	0.9476	0.9554	0.9559	0.9561
Standard deviation (σ)	0.0248	0.0219	0.0235	0.0229	0.0223

Table 4. Inter-distance distribution of Np6A/Np6 patterns.

Group size (samples)	1 × 1 (1099)	2 × 2 (768)	3 × 3 (264)	4 × 4 (132)	5 × 5 (88)
Mean (μ)	0.3316	0.2457	0.2327	0.2295	0.2332
Standard deviation (σ)	0.0444	0.0397	0.0391	0.0364	0.0339

Table 5. Intra-distance distribution of Np6A/Np6 patterns.

Group size (samples)	1 × 1 (1099)	2 × 2 (768)	3 × 3 (264)	4 × 4 (132)	5 × 5 (88)
Mean (μ)	0.9852	0.9853	0.9843	0.9845	0.9847
Standard deviation (σ)	0.0188	0.0134	0.0121	0.0108	0.0108

Table 6. Cut-off threshold and false positive/negative rates of DDT patterns.

Group size	1 × 1	2 × 2	3 × 3	4 × 4	5 × 5
Cut-off threshold	0.8128	0.7352	0.6379	0.5939	0.5719
False-positive rate	1.585×10^{-7}	1.511×10^{-23}	3.844×10^{-43}	5.248×10^{-58}	4.222×10^{-68}
False-negative rate	3.293×10^{-4}	3.199×10^{-20}	4.537×10^{-40}	2.732×10^{-55}	1.458×10^{-65}

Table 7. Cut-off threshold and false positive/negative rates of Np6A/Np6 patterns.

Group size	1 × 1	2 × 2	3 × 3	4 × 4	5 × 5
Cut-off threshold	0.7898	0.7978	0.8055	0.8115	0.8030
False-positive rate	1.150×10^{-25}	1.034×10^{-44}	2.430×10^{-49}	3.106×10^{-58}	5.826×10^{-64}
False-negative rate	3.428×10^{-25}	3.619×10^{-44}	8.444×10^{-49}	1.186×10^{-57}	1.747×10^{-63}

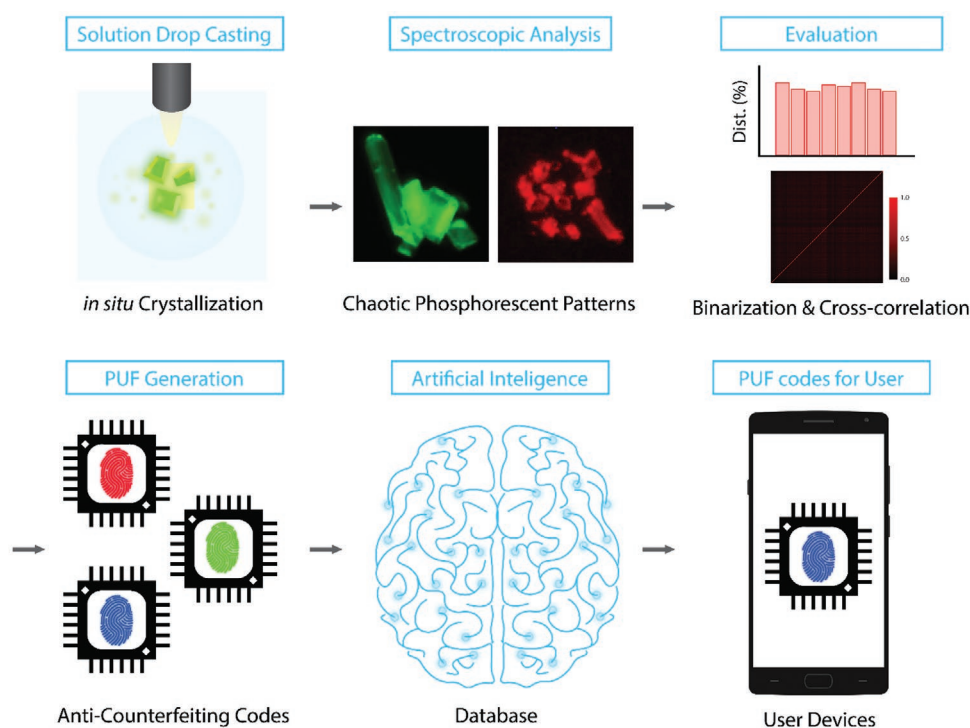


Figure 6. Proposed authentication process using chaotic phosphorescent pattern PUFs.

function and binarized with the “im2bw” function. Here, objects less than 25-pixel size were removed with the “bwareaopen” function to prevent residual dust influences. Then, individual organic crystals and the number of crystals per MoS₂ seeds were classified by the “bwlabel” function. Besides, the “regionprops” function elicited morphological features. It possesses various attribute values and properties; “Area” for the region size, “MinorAxisLength” and “MajorAxisLength” for the aspect ratio, and “Orientation” for the heading angle. For the location analysis where organic crystals were formed, thousands of extracted individual binary images were applied. The position probabilities were obtained for each location by calculating the average value through the “mean” function after sorting and combining all the individual binarized images.

2D Cross-Correlation Process: A pattern should be perceived as identical even in different environmental conditions. Thus, each pattern was photographed twice for binarized images. In addition, it was demagnified by 5 times through the “imresize” function. A weighted averaging filter was automatically applied by the “bicubic” method as a default. By applying 3 × 3 size 2D Kernel Filters, vertical

([−1 0 1; −2 0 2; −1 0 1]), horizontal ([−1 −2 −1; 0 0 0; 1 2 1]), and diagonal ([−2 −1 0; −1 0 1; 0 1 2], [0 −1 −2; 1 0 −1; 2 1 0]) orientation, in the “conv2” function, the crystal edges were directionally classified. Then, it was analyzed by the “normxcorr2” function and normalized cross-correlation method to determine the uniqueness.

Supporting Information

Supporting Information is available from the Wiley Online Library or from the author.

Acknowledgements

This research was supported by the Basic Science Research Program through the National Research Foundation of Korea (NRF)

(2021R1A2B5B02002167, 2021R1A4A5031805, 2021R11A1A01047275, and 2018R1A6A1A03025708).

Conflict of Interest

The authors declare no conflict of interest.

Data Availability Statement

Research data are not shared.

Keywords

MoS₂, organic crystal patterns, physical unclonable functions, security labels

Received: April 2, 2021

Revised: June 22, 2021

Published online: September 12, 2021

-
- [1] V. van der Leest, P. Tuyls, in *2013 Design, Automation & Test in Europe Conf. & Exhibition (DATE)*, IEEE, Piscataway, NJ, USA **2013**, pp. 1137–1142, <https://doi.org/10.7873/DATE.2013.238>.
- [2] Z. Hu, J. M. M. L. Comeras, H. Park, J. Tang, A. Afzali, G. S. Tulevski, J. B. Hannon, M. Liehr, S.-J. Han, *Nat. Nanotechnol.* **2016**, *11*, 559.
- [3] J. Zhang, K. L. McCann, C. Qiu, L. E. Gonzalez, S. J. Baserga, T. M. T. Hall, *Nat. Commun.* **2016**, *7*, 13085.
- [4] R. Pappu, *Science* **2002**, *297*, 2026.
- [5] M. R. Carro-Temboury, R. Arppe, T. Vosch, T. J. Sørensen, *Sci. Adv.* **2018**, *4*, e1701384.
- [6] T. Takahashi, Y. Kudo, R. Ishiyama, in *2017 Fifteenth IAPR Int. Conf. on Machine Vision Applications (MVA)*, IEEE, Piscataway, NJ, USA **2017**, pp. 202–206, <https://doi.org/10.23919/MVA.2017.7986836>.
- [7] R. Horstmeyer, B. Judkewitz, I. M. Vellekoop, S. Assaworrorat, C. Yang, *Sci. Rep.* **2013**, *3*, 3543.
- [8] B. Wigger, T. Meissner, A. Förste, V. Jetter, A. Zimmermann, *Sci. Rep.* **2018**, *8*, 4738.
- [9] Y. Geng, J. Noh, I. Drevensek-Olenik, R. Rupp, G. Lenzini, J. P. F. Lagerwall, *Sci. Rep.* **2016**, *6*, 26840.
- [10] R. Arppe, T. J. Sørensen, *Nat. Rev. Chem.* **2017**, *1*, 0031.
- [11] Y. Gao, S. F. Al-Sarawi, D. Abbott, *Nat. Electron.* **2020**, *3*, 81.
- [12] X. Xu, A. Rahmati, D. E. Holcomb, K. Fu, W. Burleson, *IEEE Trans. Comput.-Aided Des. Integr. Circuits Syst.* **2015**, *34*, 903.
- [13] D. E. Holcomb, W. P. Burleson, K. Fu, *IEEE Trans. Comput.* **2009**, *58*, 1198.
- [14] J. W. Leem, M. S. Kim, S. H. Choi, S.-R. Kim, S.-W. Kim, Y. M. Song, R. J. Young, Y. L. Kim, *Nat. Commun.* **2020**, *11*, 328.
- [15] Y. Liu, F. Han, F. Li, Y. Zhao, M. Chen, Z. Xu, X. Zheng, H. Hu, J. Yao, T. Guo, W. Lin, Y. Zheng, B. You, P. Liu, Y. Li, L. Qian, *Nat. Commun.* **2019**, *10*, 2409.
- [16] H. Minemawari, T. Yamada, H. Matsui, J. Tsutsumi, S. Haas, R. Chiba, R. Kumai, T. Hasegawa, *Nature* **2011**, *475*, 364.
- [17] W. Wang, L. Wang, G. Dai, W. Deng, X. Zhang, J. Jie, X. Zhang, *Nano-Micro Lett.* **2017**, *9*, 52.
- [18] Q. Wang, E. J. Juarez-Perez, S. Jiang, L. Qiu, L. K. Ono, T. Sasaki, X. Wang, Y. Shi, Y. Zheng, Y. Qi, Y. Li, *J. Phys. Chem. Lett.* **2018**, *9*, 1318.
- [19] J. Jang, S. Nam, K. Im, J. Hur, S. N. Cha, J. Kim, H. Bin Son, H. Suh, M. A. Loth, J. E. Anthony, J.-J. Park, C. E. Park, J. M. Kim, K. Kim, *Adv. Funct. Mater.* **2012**, *22*, 1005.
- [20] A. L. Briseno, S. C. B. Mannsfeld, M. M. Ling, S. Liu, R. J. Tseng, C. Reese, M. E. Roberts, Y. Yang, F. Wudl, Z. Bao, *Nature* **2006**, *444*, 913.
- [21] H. Wang, F. Fontein, J. Li, L. Huang, L. Jiang, H. Fuchs, W. Wang, Y. Wang, L. Chi, *ACS Appl. Mater. Interfaces* **2020**, *12*, 48854.
- [22] Y. Lee, J. Lee, H. Bark, I.-K. Oh, G. H. Ryu, Z. Lee, H. Kim, J. H. Cho, J.-H. Ahn, C. Lee, *Nanoscale* **2014**, *6*, 2821.
- [23] O. Bolton, K. Lee, H.-J. Kim, K. Y. Lin, J. Kim, *Nat. Chem.* **2011**, *3*, 205.
- [24] E. Cho, J. Choi, S. Jo, D. Park, Y. K. Hong, D. Kim, T. S. Lee, *ChemPlusChem* **2019**, *84*, 1130.
- [25] A. K. Singh, P. Kumar, D. J. Late, A. Kumar, S. Patel, J. Singh, *Appl. Mater. Today* **2018**, *13*, 242.
- [26] J. Liu, C. Zhu, K. Liu, Y. Jiang, Y. Song, J. S. Francisco, X. C. Zeng, J. Wang, *Proc. Natl. Acad. Sci. USA* **2017**, *114*, 11285.
- [27] E. Sawicki, H. Johnson, *Microchem. J.* **1964**, *8*, 85.
- [28] D. R. Kearns, W. A. Case, *J. Am. Chem. Soc.* **1966**, *88*, 5087.
- [29] H. Ma, H. Yu, Q. Peng, Z. An, D. Wang, Z. Shuai, *J. Phys. Chem. Lett.* **2019**, *10*, 6948.
- [30] F. Kobayashi, R. Ohtani, S. Teraoka, M. Yoshida, M. Kato, Y. Zhang, L. F. Lindoy, S. Hayami, M. Nakamura, *Chem. - Eur. J.* **2019**, *25*, 5875.
- [31] A. M. J. van Eijk, G. B. Ekelmans, W. Klinkenberg, A. H. Huizer, C. A. G. O. Varma, *J. Chem. Soc., Faraday Trans.* **1990**, *86*, 2083.